Band Engineering of Large-Twist-Angle Graphene/*h*-BN Moiré Superlattices with Pressure

Yang Gao,[1,2,3] Xianqing Lin,[4] Thomas Smart,[5] Penghong Ci,[1,2] Kenji Watanabe,[6] Takashi Taniguchi,[7] Raymond Jeanloz,[5] Jun Ni,[8] and Junqiao Wu[1,2,*]

[1]*Department of Materials Science and Engineering, University of California, Berkeley, California 94720, USA*
[2]*Materials Sciences Division, Lawrence Berkeley National Laboratory, Berkeley, California 94720, USA*
[3]*Department of Engineering Mechanics, Zhejiang University, Hangzhou 310027, People's Republic of China*
[4]*College of Science, Zhejiang University of Technology, Hangzhou 310023, People's Republic of China*
[5]*Department of Earth and Planetary Science, University of California, Berkeley, California 94720, USA*
[6]*Research Center for Functional Materials, National Institute for Materials Science, 1-1 Namiki, Tsukuba 305-0044, Japan*
[7]*International Center for Materials Nanoarchitectonics, National Institute for Materials Science, 1-1 Namiki, Tsukuba 305-0044, Japan*
[8]*State Key Laboratory of Low-Dimensional Quantum Physics and Frontier Science Center for Quantum Information, Department of Physics, Tsinghua University, Beijing 100084, People's Republic of China*

(Received 17 May 2020; accepted 22 September 2020; published 25 November 2020)

Graphene interfacing hexagonal boron nitride (*h*-BN) forms lateral moiré superlattices that host a wide range of new physical effects such as the creation of secondary Dirac points and band gap opening. A delicate control of the twist angle between the two layers is required as the effects weaken or disappear at large twist angles. In this Letter, we show that these effects can be reinstated in large-angle (∼1.8°) graphene/*h*-BN moiré superlattices under high pressures. A graphene/*h*-BN moiré superlattice microdevice is fabricated directly on the diamond culet of a diamond anvil cell, where pressure up to 8.3 GPa is applied. The band gap at the primary Dirac point is opened by 40–60 meV, and fingerprints of the second Dirac band gap are also observed in the valence band. Theoretical calculations confirm the band engineering with pressure in large-angle graphene/*h*-BN bilayers.

DOI: 10.1103/PhysRevLett.125.226403

van der Waals (vdW) heterostructures by vertically stacking two-dimensional (2D) materials exhibit emergent properties distinct from those of the individual 2D layers [1–11]. For example, the periodic moiré potential imposed on monolayer graphene (MLG) by interfacing hexagonal Boron Nitride (*h*-BN) with delicately controlled rotational-angle alignment breaks the inversion symmetry and opens a band gap at the primary Dirac point (PDP) as well as a series of secondary Dirac band gaps in both the valence and conduction bands [12–15]; bilayer graphene with a "magic" twist angle of ∼1.1° shows Mott-insulating behavior at half filling and superconductivity if doped by electric fields [16–18]. All these novel effects emerge only at very small, sometimes specific, twist angles between neighboring layers, which imposes an experimental challenge.

Interests are growing in the role that interlayer vdW forces play in regulating these emergent effects in vdW structures [19–22]. A recent study by Yankowitz *et al.* reports that hydrostatic pressure is powerful in tuning the interlayer coupling and hence band structures of graphene moiré superlattices [20]. The band gap at the PDP of 0.6° twisted moiré superlattices was raised from 30 meV at ambient to 50 meV at 2.3 GPa applied in a piston cell. Wider band gaps are intuitively expected in the graphene system under higher pressures, and also of importance for electronics applications. However, the maximum pressure is typically limited to be below ∼3 GPa in piston cells. In contrast, diamond anvil cells (DACs) can generate extremely high hydrostatic pressures (up to ∼1 TPa), and they are widely used to tune the interlayer spacing of 2D materials. However, DACs are typically used to carry out nonelectrical experiments of ultrathin (few-layer) 2D materials such as Raman and photoluminescence [23–27] due to daunting technical difficulties in electrical wiring of atomically thin materials through the DAC [28,29]. A limited number of electrical measurements in DAC reveal unusual properties of ultrathin 2D materials at high pressures, such as much improved electron mobility in few-layer MoS_2 [28]. Therefore, it is intriguing to search for new electronic properties of graphene moiré superlattices at high pressures in a DAC. The electron-beam lithography (along with one-dimensional edge contact) commonly used for microdevice fabrication of vdW materials [30] is not compatible with the DAC, as the diamond is insulating and the epoxy (for fixing the diamond) is vulnerable to electron beams. Chen *et al.*[28] developed a new method to prepare and measure field effect transistors (FETs) of MoS_2 in a DAC by directly lithographically patterning microdevices onto the diamond culet. In this work, we advance this method to fabricate and measure three-terminal FETs of graphene moiré superlattices in the DAC.

For the graphene/h-BN moiré superlattices, experimental and theoretical studies have demonstrated the significance and sensitivity of the rotational alignment between the two layers [31–37]. For example, the band gap near the PDP is around 30 meV if the twist angle is $<2°$ and progressively decreases if the twist angle increases. The band gap at the secondary Dirac points (SDPs) rapidly decreases when the twist angle increases and vanishes when the twist angle is $>1°$ [31]. Most recent studies of graphene/h-BN moiré superlattices are focused on systems with small twist angles ($< \sim 1°$), since most of the intriguing physical phenomena are believed to appear only in these well-aligned systems. However, making a nearly perfectly aligned graphene/h-BN stack is extremely challenging even for very experienced hands and the possible exotic properties of systems with large twist angles remain nearly unexplored. In this work, electrical transport measurements are carried out on graphene/h-BN moiré superlattices with a rather large twist angle of $\sim 1.8°$. We show that the PDP band gap increases by 40–60 meV at a pressure of 8.3 GPa. Theoretical calculations confirm these findings and further predict that an indirect band gap opens at the SDP in the valence band when pressure exceeds 7.3 GPa, and reaches 4.7 meV at 8.4 GPa. Experimental fingerprints are observed to be consistent with the prediction about the secondary band gap.

Figures 1(a) and 1(b) illustrate our experimental setup. Cubic-BN (c-BN) mixed with epoxy gel was coated onto a stainless-steel gasket to avoid shorting between electrodes. Ruby particles were used for pressure calibration. A bar-shaped, ~50 nm thick graphite flake was first transferred onto the diamond culet (~300 μm in diameter) as the bottom gate. The dielectric h-BN and drain-source graphite flakes were then sequentially transferred onto the bottom graphite. The graphite flakes serve as part of the drain and source electrodes to extend the contacts to graphene, so that metal-electrode deposition could be done in the final step once for all to minimize the damage and enhance the yield. A monolayer graphene was aligned with and picked up by a top h-BN flake (~40–80 nm thick) to obtain the moiré superlattices. Mechanically exfoliated graphene and h-BN tend to break along the zigzag or armchair axis. Therefore, the key to obtain a precisely controlled alignment is to optically identify MLG and h-BN flakes with straight edges and match the straight edges in the pickup process. A rotational stage was incorporated to provide the degree of freedom of controlling the relative alignment. The alignment angle was then estimated from the width of the Raman 2D peak as it is quantitatively established that a smaller-angle alignment leads to a wider Raman 2D peak [38]. More details about the twist-angle determination and the discussions of the possible experimental artifacts are in the Supplemental Material [39]. Then the graphene/h-BN stack was carefully transferred onto the dielectric h-BN. It is noted that the MLG was intentionally misaligned with the bottom dielectric h-BN layer, such that the moiré superlattices are defined only by the alignment angle of the MLG with the top h-BN. The MLG was then well protected by the two encapsulating h-BN layers [59]. Importantly, transferring of the aligned graphene/h-BN bilayer requires extremely careful positioning, such that the MLG is in contact with both the drain and source graphite flakes. All the 2D flakes were transferred using the conventional polymer-assisted dry transfer method to ensure clean interfaces [33,60]. The device was carefully sonicated in acetone after each transfer to remove the polymer residues and the surface cleanliness was confirmed with atomic force microscopy. Afterward, three blocks of Au/Ti (70 nm/8 nm) were patterned using photolithography and deposited as gate-drain-source electrodes onto the corresponding graphite flakes. Finally, narrow strips of Pt foil (~5 μm thick) were manually mounted onto each Au/Ti electrode as feedthrough wires to external electronics. The actual fabrication process is summarized in Fig. 1(d). More details about the fabrication process are in the Supplemental Material [39]. This is a general and feasible device fabrication strategy that can be applied to preparation of other vdW heterostructure microdevices in the DAC. Figure 2(a) shows current-voltage (I-V) characteristics of the $\sim 1.8°$ twisted graphene/h-BN FET measured in the DAC at room temperature. The drain-source graphite flakes provide excellent Ohmic contact, as shown in Fig. 2(a). The I-V curves at different pressures all display good linearity, proving robustness of the FET device under high pressure.

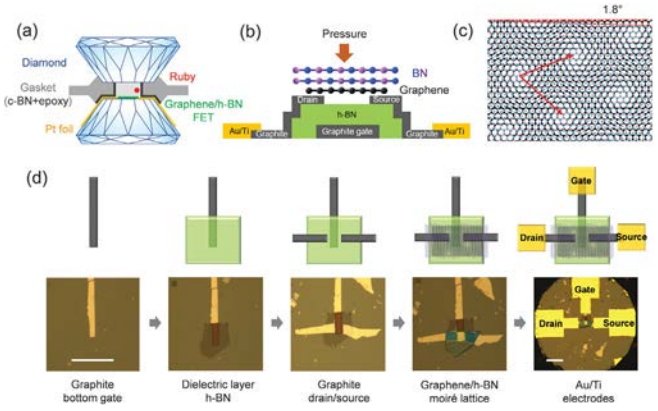

FIG. 1. Experiment schematic and fabrication process of the graphene/h-BN field effect transistor in DAC. (a) A schematic of the experimental setup. The graphene/h-BN field effect transistor is directly fabricated on the diamond culet and sealed inside the gasket chamber. Pt foils are manually mounted as feedthrough wires. The pressure is calibrated by ruby particles. (b) Schematic side view of the device. Graphite flakes are used as part of the electrodes. (c) A cartoon showing the graphene/h-BN moiré superlattices with twist angle of $\sim 1.8°$. The red lines indicate the moiré wavelength. (d) Fabrication process of the device. All the 2D flakes are dry transferred. The diamond culet size is 300 μm and the scale bars are 50 μm.

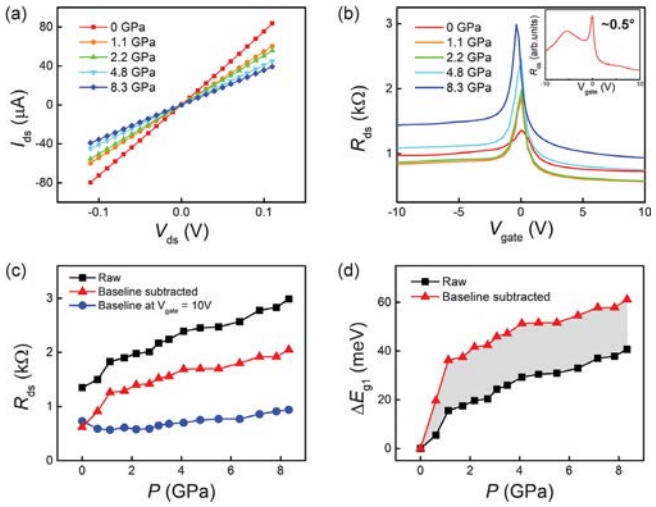

FIG. 2. Transport measurements of the ~1.8° twisted graphene/h-BN FET in DAC. (a) Two-probe I-V curves of the FET in DAC. (b) Transfer curves of the same device in the DAC. Inset: transfer curve of a smaller-angle (0.5°) twisted graphene/h-BN device recorded at ambient pressure. Clear electron-hole asymmetry is shown in both small and large twist-angle systems. (c) Drain-source resistance at the primary Dirac point, baseline resistance (at $V_{gate} = 10$ V) and the baseline-subtracted resistance at the primary Dirac point, under different pressures. (d) Pressure induced PDP band gap opening ΔE_{g1} with respect to the band gap at ambient pressure. The shadow area indicates the possible PDP band gap widening range considering the contact resistance.

Shown in Fig. 2(b) is the channel resistance (R_{ds}) of the FET as a function of gate voltage (V_{gate}) under different pressures. The peak near zero gate voltage is associated with the PDP, which increases from 1.3 kΩ at ambient pressure to 3 kΩ at 8.3 GPa, suggesting opening of a band gap (E_{g1}) at the PDP by the pressure. Another critical effect in Fig. 2(b) is the asymmetry of the baseline resistance under positive vs negative gate voltages. We have tested four other FETs with different twist angles and all FETs show such asymmetry. When the twist angle is small, the SDP shows up as a broad peak at both positive and negative V_{gate}, corresponding to the band gap of the SDP in the conduction and valence band, respectively [31]. This is also shown in the inset for a ~0.5° aligned graphene/h-BN FET measured at ambient pressure and room temperature. It is clear that the SDP peak in the valence band is much stronger than in the conduction band. This asymmetry has been observed in previous experiments [12–14,31], and theoretically attributed to the difference between the wave functions in the conduction-valence bands combined with the inversion asymmetry introduced by the h-BN layer [34,36,61–63]. The inversion asymmetry creates two correlated terms in the perturbed Hamiltonian: the honeycomb sublattice site energy term and the intersublattice hopping term. These two sublattice-related terms will cancel (in the conduction band) or add up (in the valence band) for the SDP gap, due to the opposite chiral convolutions of the bands. The SDPs will be broadened by temperature, disorder, and inhomogeneities, lifting up the baseline resistance between the PDP and the SDPs. As a consequence, the baseline of R_{ds} for negative V_{gate} (valence band) is usually higher than for the positive V_{gate} (conduction band). For this reason, we believe the asymmetric baseline in Fig. 2(b) is the residue of the SDPs in the case of large twist angles, and implies that moiré superlattices have indeed formed in the graphene. The SDP band gap is further discussed in conjunction with theoretical calculations.

It is noted that R_{ds} of our FETs was measured in a two-terminal configuration, so contact resistance is expected. However, one could estimate the lower limit of the real PDP peak resistance by subtracting the raw data with the baseline resistance, which can be taken at $V_{gate} = 10$ V where R_{ds} no longer changes with V_{gate}. The raw PDP peak resistance, baseline resistance at $V_{gate} = 10$ V, and the baseline-subtracted PDP peak resistance are plotted as a function of pressure in Fig. 2(c). Next, we use the PDP peak resistance to extract the band gap opening by using the Arrhenius dependence [20]:

$$\sigma = Ae^{-(E_{g1}/2k_BT)}, \tag{1}$$

where σ is the channel conductivity calculated from R_{ds}, and A is the coefficient. Although all our measurements were done at room temperature, previous reports [20] have shown that the plot of $\ln\sigma$ vs $1/T$ of graphene/h-BN moiré superlattices is linear under different pressures. More importantly, all the $\ln\sigma$ vs $1/T$ lines under different pressures tend to converge onto a single point on the $\ln\sigma$ axis, indicating that $\ln A$ is nearly pressure independent. Therefore, we estimate the change in E_{g1} with respect to E_{g1} in ambient pressure,

$$\Delta E_{g1} = -2k_BT * \ln\left(\frac{\sigma}{\sigma_0}\right), \tag{2}$$

where σ_0 is the PDP peak resistance at ambient pressure.

The extracted ΔE_{g1} values are plotted as a function of pressure in Fig. 2(d), where the values obtained from both raw R_{ds} and baseline-subtracted R_{ds} are shown. The actual ΔE_{g1} should lie between these bounds, as shown by the shaded area. The band gap at the PDP is expanded by 40–60 meV at 8.3 GPa. Using the previously reported experimental value of E_{g1} ~30 meV [31] for similar twist angles at ambient pressure, the final E_{g1} at 8.3 GPa is between 70 and 90 meV, enhanced by 2–3 times over the ambient value. Data above 8.3 GPa are not included here because h-BN undergoes a structural phase transition to c-BN at about 9 GPa, resulting in destruction of the moiré superlattices. The complete set of transport data is in Fig. S3.

To better probe the physical origin of the band gap opening in large-twist-angle graphene moiré superlattices, we performed theoretical calculations using models with inputs from *ab initio* density functional theory (DFT) computation. Fully relaxing the graphene/h-BN structure with a twist angle of ∼1.8° and a fixed average interlayer space (h_0), the equilibrium pressure (P) at given h_0 is obtained and illustrated in Fig. S4. Subjecting to high pressures up to 10 GPa, the equilibrium h_0 is significantly reduced in the graphene/h-BN bilayer. The band structure of the relaxed graphene/h-BN under pressure was calculated by employing the effective lattice model of the moiré superlattices in graphene with the Hamiltonian,

$$H = \sum_i (H_{A,i} c^\dagger_{A,i} c_{A,i} + H_{B,i} c^\dagger_{B,i} c_{B,i}) - \sum_i \sum_{n=1}^{3} t_{n,i} (c^\dagger_{A,i} c_{B,i,n} + c^\dagger_{B,i,n} c_{A,i}), \quad (3)$$

where $c^\dagger_{\alpha,i} (\alpha = A, B)$ is the creation and $c_{\alpha,i}$ is the annihilation operator of a p_z-like state at the site in the sublattice α and unit cell i of the MLG hexagonal lattice, $c^\dagger_{B,i,n}$ and $c_{B,i,n}$ are operators at the nearest sites of the sublattice-A atom in cell i, and the on-site energies and hopping terms are represented by $H_{\alpha,i}$ and $-t_{n,i}$, respectively. The hopping and on-site terms at a site with a local shift vector $\boldsymbol{d}$ are expanded in Fourier series with the expansion parameters decaying exponentially with the local interlayer spacings as described in Supplemental Material [39]. For the considered system twisted by ∼1.8°, only a small gap of $E_{g1} = 8$ meV is opened at the PDP at ambient pressure, and bands around the SDPs in both the valence and conduction bands are significantly overlapped, as seen in Fig. 3(a) and Fig. S5(a) in the Supplemental Material [39]. Since this twisted system has a much smaller moiré supercell (moiré wavelength ∼4 nm) compared to the perfectly aligned system (moiré wavelength ∼14 nm), the sublattice asymmetry and the in-plane structural deformation are much less pronounced, leading to the smaller PDP gap [36,37]. With increasing pressure, the interlayer spacing decreases and the energy differences between domains with different stackings grow, resulting in stronger in-plane structural relaxation and larger domains with energetically favored stacking. Consequently, the sublattice asymmetry in the Hamiltonian becomes stronger, and the gap at the PDP increases. The calculated PDP gap (E_{g1}) vs pressure is plotted in Fig. 3(a), along with the experimentally evaluated band gap range. The calculated E_{g1} rises from 8 meV at ambient to 50 meV at 8.4 GPa, as shown in Fig. 3(a). The gap opening of $\Delta E_{g1} = 42$ meV is in good agreement with the experimental value. The band structures near the PDP at 0, 4.9, and 8.4 GPa are also plotted in Fig. 3(b). The gap is continuously opened by pressure whereas away from the gap the linear dispersion stays. Therefore, both experiments and calculations

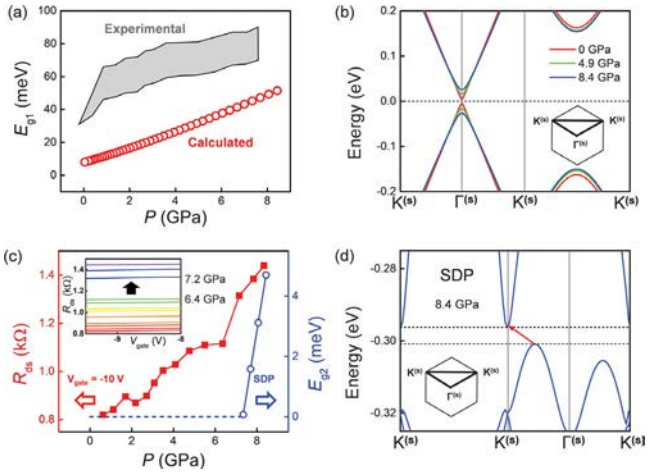

FIG. 3. Calculations of the band structure of the ∼1.8° twisted system. (a) the calculated and experimental band gap at the PDP vs pressure. The red circles depict the band gap evolution obtained from theoretical calculations and the gray area is the estimated band gap range from Fig. 2(d) using the gap value of 30 meV at 0 GPa from Ref. [31]. (b) Calculated band structure near the PDP at 0 GPa, 4.9 GPa, and 8.4 GPa, respectively. Inset: the $\boldsymbol{k}$ path in the moiré Brillouin zone. (c) Calculated gap near the SDP in valence band and the drain-source resistance at $V_{\text{gate}} = -10$ V as a function of pressure. Blue dashed line indicates overlapped bands (i.e., zero gap). Inset: raw resistance data at $V_{\text{gate}} = -8$ V to -10 V. A none-zero SDP gap emerges at 7.3 GPa and an abrupt resistance increase on the hole side is also observed near 7 GPa. (d) Band structure near the SDPs in the valence band at 8.4 GPa. An indirect gap of 4.7 meV is opened.

demonstrate that high pressure is an effective tool to open the band gap of graphene/h-BN moiré superlattices even at rather large twist angle.

Moreover, in contrast to small-twist-angle systems that show a sizable direct gap at the SDP in the valence band, the bands around the SDPs now overlap due to the much weaker moiré potential, as shown in Fig. S5. The hydrostatic pressure reduces the band overlapping around the SDPs in the valence band and eventually opens an indirect gap (E_{g2}). The band gap opening at the SDPs is due to the enhanced moiré potential caused by the pressure, as the Hamiltonian parameters increase exponentially with decreasing interlayer spacing (details in Supplemental Material [39]). As shown in Fig. 3(c), under pressures higher than a critical value of 7.3 GPa, an indirect gap emerges in the valence band around the SDPs, and keeps increasing to a small but non-negligible value of 4.7 meV at 8.4 GPa. Even considering the usual underestimate of the band gap given by first-principle calculations, the indirect secondary gap of the ∼1.8° system is likely to be quite narrow, which can explain why the SDPs in the large-twist-angle system have not been experimentally reported in previous studies. The narrow and indirect secondary gap is likely to generate a rather weak and broad secondary Dirac peak on the hole side, leading to a moderately flat baseline

[instead of an upward shape like the inset in Fig. 2(b)] even at high pressure. Interestingly, the resistance R_{ds} at $V_{gate} = -10$ V (probing the valence band) shows an abrupt rise at the pressure of about 7 GPa, as plotted also in the inset of Fig. 3(c). As illustrated both in the literature [31] as well as in Fig. 2(b), the hole side R_{ds} is a qualitative measure of the SDP peak resistance. Therefore, the abrupt rise of the hole side R_{ds} near 7 GPa is likely an experimental fingerprint to trace the SDP gap opening. The band structure near the SDPs in the valence band at 8.4 GPa is plotted in Fig. 3(d). Our calculations of the system show that the gap at the SDPs remains indirect even when the pressure reaches 16.4 GPa (Fig. S6). The indirect feature of the SDP gap could be attributed to the rather small moiré supercell in the considered graphene/h-BN structure, which makes the dispersion of the band right below the SDPs insensitive to pressure. It is also noted that pressure cannot open the SDP gap in the conduction band even at 16.4 GPa, as shown in Fig. S6, further testifying the particle-hole asymmetry in the system.

In conclusion, we demonstrate that large-twist-angle graphene/h-BN moiré superlattices can also host emergent electronic physics under mildly high pressures. For ~1.8° twisted superlattices, the band gap at the primary Dirac point is opened to ~70–90 meV at a pressure of 8.3 GPa. Therefore, we show that poorly aligned graphene/h-BN moiré superlattices can also serve as a platform for exotic physical effects, adding more freedom in preparation and investigation of graphene moiré superlattices. We also for the first time theoretically predict and experimentally trace the fingerprint of the secondary Dirac gap opened by pressure in large-twisted graphene superlattices, providing opportunities for a wide range tuning of the moiré electronics with pressure. The work shows that pressure can effectively unlock and control moiré physics in graphene superlattices, and similar tool could be used to probe emerging physics in heterostructures of transition metal chalcogenides.

This work was supported by U.S. NSF Grant No. DMR-1708448. R. J. acknowledges funding from CMEC (DOE NNSA Award DE-NA-0003842). The theoretical calculations were supported by the National Natural Science Foundation of China (Grants No. 11974312 and No. 11774195) and the National Key Research and Development Program of China (Grant No. 2016YFB0700102). The materials preparation was partly supported by the Elemental Strategy Initiative conducted by the MEXT, Japan (Grant No. JPMXP0112101001), JSPS KAKENHI (Grant No. JP20H00354) and the CREST (JPMJCR15F3), JST. The device fabrication part used facilities in the Electronic Materials Program in the Lawrence Berkeley National Laboratory funded by the Director, Office of Science, Office of Basic Energy Sciences, Materials Sciences and Engineering Division, of the U.S. Department of Energy under Contract No. DE-AC02-05CH11231. The laser milling of pressure gasket was done at the Beamline 12.2.2 of Advanced Light Source at the Lawrence Berkeley National Laboratory, under support of COMPRES, the Consortium for Materials Properties Research in Earth Sciences, under NSF Cooperative Agreement EAR 1606856. We gratefully thank Dr. Jinyan Yuan (Advanced Light Source) and Dr. Feng Ke (Stanford University) for help on the preparation of insulating gaskets.

J. W. conceived the work. Y. G. conducted the experiments and data acquisition. X. L and J. N. developed the theory and performed the *ab initio* calculations. P. C., T. S., and R. J. contributed to device and DAC preparations. K. W. and T. T. prepared the h-BN crystal. J. W., Y. G., X. L., and R. J. participated in writing the paper.

*Corresponding author.
wuj@berkeley.edu

[1] A. K. Geim and I. V. Grigorieva, Nature (London) **499**, 419 (2013).
[2] K. S. Novoselov, A. Mishchenko, A. Carvalho, and A. H. Castro Neto, Science **353**, aac9439 (2016).
[3] M. Yankowitz, Q. Ma, P. Jarillo-Herrero, and B. J. LeRoy, Nat. Rev. Phys. **1**, 112 (2019).
[4] B. Hunt *et al.*, Science **340**, 1427 (2013).
[5] C. R. Dean *et al.*, Nature (London) **497**, 598 (2013).
[6] L. Wang, Y. Gao, B. Wen, Z. Han, T. Taniguchi, K. Watanabe, M. Koshino, J. Hone, and C. R. Dean, Science **350**, 1231 (2015).
[7] C. Woods *et al.*, Nat. Phys. **10**, 451 (2014).
[8] X. Hong, J. Kim, S.-F. Shi, Y. Zhang, C. Jin, Y. Sun, S. Tongay, J. Wu, Y. Zhang, and F. Wang, Nat. Nanotechnol. **9**, 682 (2014).
[9] C. Jin *et al.*, Nature (London) **567**, 76 (2019).
[10] K. L. Seyler, P. Rivera, H. Yu, N. P. Wilson, E. L. Ray, D. G. Mandrus, J. Yan, W. Yao, and X. Xu, Nature (London) **567**, 66 (2019).
[11] K. Tran *et al.*, Nature (London) **567**, 71 (2019).
[12] M. Yankowitz, J. Xue, D. Cormode, J. D. Sanchez-Yamagishi, K. Watanabe, T. Taniguchi, P. Jarillo-Herrero, P. Jacquod, and B. J. LeRoy, Nat. Phys. **8**, 382 (2012).
[13] L. Ponomarenko *et al.*, Nature (London) **497**, 594 (2013).
[14] E. Wang *et al.*, Nat. Phys. **12**, 1111 (2016).
[15] Z.-G. Chen, Z. Shi, W. Yang, X. Lu, Y. Lai, H. Yan, F. Wang, G. Zhang, and Z. Li, Nat. Commun. **5**, 4461 (2014).
[16] Y. Cao *et al.*, Nature (London) **556**, 80 (2018).
[17] Y. Cao, V. Fatemi, S. Fang, K. Watanabe, T. Taniguchi, E. Kaxiras, and P. Jarillo-Herrero, Nature (London) **556**, 43 (2018).
[18] Y. Cao, D. Rodan-Legrain, O. Rubies-Bigorda, J. M. Park, K. Watanabe, T. Taniguchi, and P. Jarillo-Herrero, Nature (London) **583**, 215 (2020).
[19] M. Yankowitz, K. Watanabe, T. Taniguchi, P. San-Jose, and B. J. LeRoy, Nat. Commun. **7**, 13168 (2016).
[20] M. Yankowitz, J. Jung, E. Laksono, N. Leconte, B. L. Chittari, K. Watanabe, T. Taniguchi, S. Adam, D. Graf, and C. R. Dean, Nature (London) **557**, 404 (2018).
[21] T. Song *et al.*, Nat. Mater. **18**, 1298 (2019).

[22] M. Yankowitz, S. Chen, H. Polshyn, Y. Zhang, K. Watanabe, T. Taniguchi, D. Graf, A. F. Young, and C. R. Dean, Science **363**, 1059 (2019).
[23] X. Li *et al.*, Appl. Phys. Lett. **109**, 242101 (2016).
[24] Y. Yan, F. Li, Y. Gong, M. Yao, X. Huang, X. Fu, B. Han, Q. Zhou, and T. Cui, J. Phys. Chem. C **120**, 24992 (2016).
[25] L. Fu *et al.*, Sci. Adv. **3**, e1700162 (2017).
[26] T. Livneh and E. Sterer, Phys. Rev. B **81**, 195209 (2010).
[27] S. Sugai and T. Ueda, Phys. Rev. B **26**, 6554 (1982).
[28] Y. Chen *et al.*, Nano Lett. **17**, 194 (2017).
[29] F. Ke, Y. Chen, K. Yin, J. Yan, H. Zhang, Z. Liu, J. S. Tse, J. Wu, H.-k. Mao, and B. Chen, Proc. Natl. Acad. Sci. U.S.A. **116**, 9186 (2019).
[30] L. Wang *et al.*, Science **342**, 614 (2013).
[31] R. Ribeiro-Palau, C. Zhang, K. Watanabe, T. Taniguchi, J. Hone, and C. R. Dean, Science **361**, 690 (2018).
[32] C. R. Woods *et al.*, Nat. Commun. **7**, 10800 (2016).
[33] K. Kim *et al.*, Nano Lett. **16**, 1989 (2016).
[34] J. Jung, A. Raoux, Z. Qiao, and A. H. MacDonald, Phys. Rev. B **89**, 205414 (2014).
[35] J. Jung, A. M. DaSilva, A. H. MacDonald, and S. Adam, Nat. Commun. **6**, 6308 (2015).
[36] J. Jung, E. Laksono, A. M. DaSilva, A. H. MacDonald, M. Mucha-Kruczyński, and S. Adam, Phys. Rev. B **96**, 085442 (2017).
[37] X. Lin and J. Ni, Phys. Rev. B **100**, 195413 (2019).
[38] A. Eckmann *et al.*, Nano Lett. **13**, 5242 (2013).
[39] See Supplemental Material at http://link.aps.org/supplemental/10.1103/PhysRevLett.125.226403 for device preparation details and full set of experimental and theoretical data, which includes Refs. [40–58].
[40] K. Kim *et al.*, Nano Lett. **16**, 1989 (2016).
[41] K. Kim, A. DaSilva, S. Huang, B. Fallahazad, S. Larentis, T. Taniguchi, K. Watanabe, B. J. LeRoy, A. H. MacDonald, and E. Tutu, Proc. Natl. Acad. Sci. U.S.A. **114**, 3364 (2017).
[42] A. Zibrov, E. Spanton, H. Zhou, C. Kometter, T. Taniguchi, K. Watanabe, and A. Young, Nat. Phys. **14**, 930 (2018).
[43] M. Yankowitz, S. Chen, H. Polshyn, Y. Zhang, K. Watanabe, T. Taniguchi, D. Graf, A. F. Young, and C. R. Dean, Science **363**, 1059 (2019).
[44] A. Eckmann *et al.*, Nano Lett. **13**, 5242 (2013).
[45] N. Funamori and T. Sato, Rev. Sci. Instrum. **79**, 053903 (2008).
[46] Y. Chen *et al.*, Nano Lett. **17**, 194 (2017).
[47] K. Yokogawa, K. Murata, H. Yoshino, and S. Aoyama, Jpn. J. Appl. Phys. **46**, 3636 (2007).
[48] A. D. Chijioke, W. J. Nellis, A. Soldatov, and I. F. Silvera, J. Appl. Phys. **98**, 114905 (2005).
[49] X. Lin and J. Ni, Phys. Rev. B **100**, 195413 (2019).
[50] X. Lin, H. Zhu, and J. Ni, Phys. Rev. B **101**, 155405 (2020).
[51] P. L. De Andres, F. Guinea, and M. I. Katsnelson, Phys. Rev. B **86**, 144103 (2012).
[52] S. Zhou, J. Han, S. Dai, J. Sun, and D. J. Srolovitz, Phys. Rev. B **92**, 155438 (2015).
[53] G. Kresse and J. Furthmüller, Comput. Mater. Sci. **6**, 15 (1996).
[54] G. Kresse and J. Furthmüller, Phys. Rev. B **54**, 11169 (1996).
[55] J. P. Perdew and A. Zunger, Phys. Rev. B **23**, 5048 (1981).
[56] P. E. Blöchl, Phys. Rev. B **50**, 17953 (1994).
[57] G. Kresse and D. Joubert, Phys. Rev. B **59**, 1758 (1999).
[58] H. J. Monkhorst and J. D. Pack, Phys. Rev. B **13**, 5188 (1976).
[59] C. R. Dean *et al.*, Nat. Nanotechnol. **5**, 722 (2010).
[60] K. Kim, A. DaSilva, S. Huang, B. Fallahazad, S. Larentis, T. Taniguchi, K. Watanabe, B. J. LeRoy, A. H. MacDonald, and E. Tutuc, Proc. Natl. Acad. Sci. U.S.A. **114**, 3364 (2017).
[61] A. M. DaSilva, J. Jung, S. Adam, and A. H. MacDonald, Phys. Rev. B **91**, 245422 (2015).
[62] J. R. Wallbank, A. A. Patel, M. Mucha-Kruczyński, A. K. Geim, and V. I. Fal'ko, Phys. Rev. B **87**, 245408 (2013).
[63] J. R. Wallbank, M. Mucha-Kruczyński, X. Chen, and V. I. Fal'ko, Ann. Phys. (Amsterdam) **527**, 359 (2015).

Supplementary Material

Band engineering of large-twist-angle graphene/h-BN moiré superlattices with pressure

Yang Gao,[1,2] Xianqing Lin,[3] Thomas Smart,[4] Penghong Ci,[1,2] Kenji Watanabe,[5] Takashi Taniguchi,[6] Raymond Jeanloz,[4] Jun Ni,[7] and Junqiao Wu[1,2,*]

[1]Department of Materials Science and Engineering, University of California, Berkeley, CA 94720, United States of America

[2]Materials Sciences Division, Lawrence Berkeley National Laboratory, Berkeley, CA 94720, United States of America

[3]College of Science, Zhejiang University of Technology, Hangzhou 310023, People's Republic of China

[4]Department of Earth and Planetary Science, University of California, Berkeley, California 94720, United States of America

[5]Research Center for Functional Materials, National Institute for Materials Science, 1-1 Namiki, Tsukuba 305-0044, Japan

[6]International Center for Materials Nanoarchitectonics, National Institute for Materials Science, 1-1 Namiki, Tsukuba 305-0044, Japan

[7]State Key Laboratory of Low-Dimensional Quantum Physics and Frontier Science Center for Quantum Information, Department of Physics, Tsinghua University, Beijing 100084, People's Republic of China

List of contents:

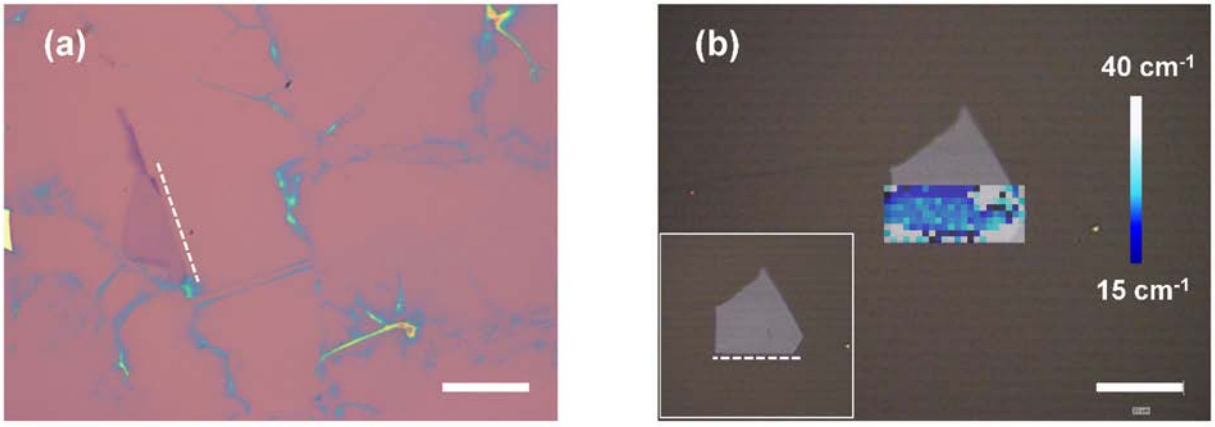

FIG. S1. Optical characterization and Raman mapping of the graphene/h-BN superlattice. (a) Optical image of the monolayer graphene. The dashed line indicates the straight crystalline edge for alignment. (b) Micro Raman mapping of the graphene 2D peak FWHM after the graphene was picked up by h-BN. The average $FWHM_{2D}$ is 25 cm^{-1}, giving a twist angle of ~1.8°. The inset is the optical image of the h-BN. The dashed line indicates the straight crystalline edge for alignment. The scale bars are 20 μm.

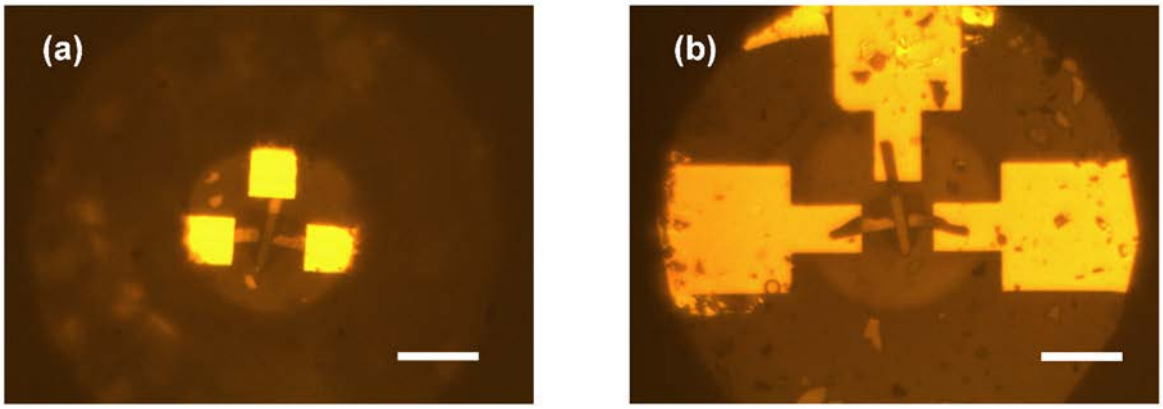

FIG. S2. Optical images of the sealed graphene moiré superlattice FET in the DAC. The left panel was taken from top-view and the right panel was taken from the bottom-view. The optical images of the device from 0 GPa to 8.3 GPa remain almost unchanged so only the images at 1 GPa are shown here. The scale bars are 50 μm.

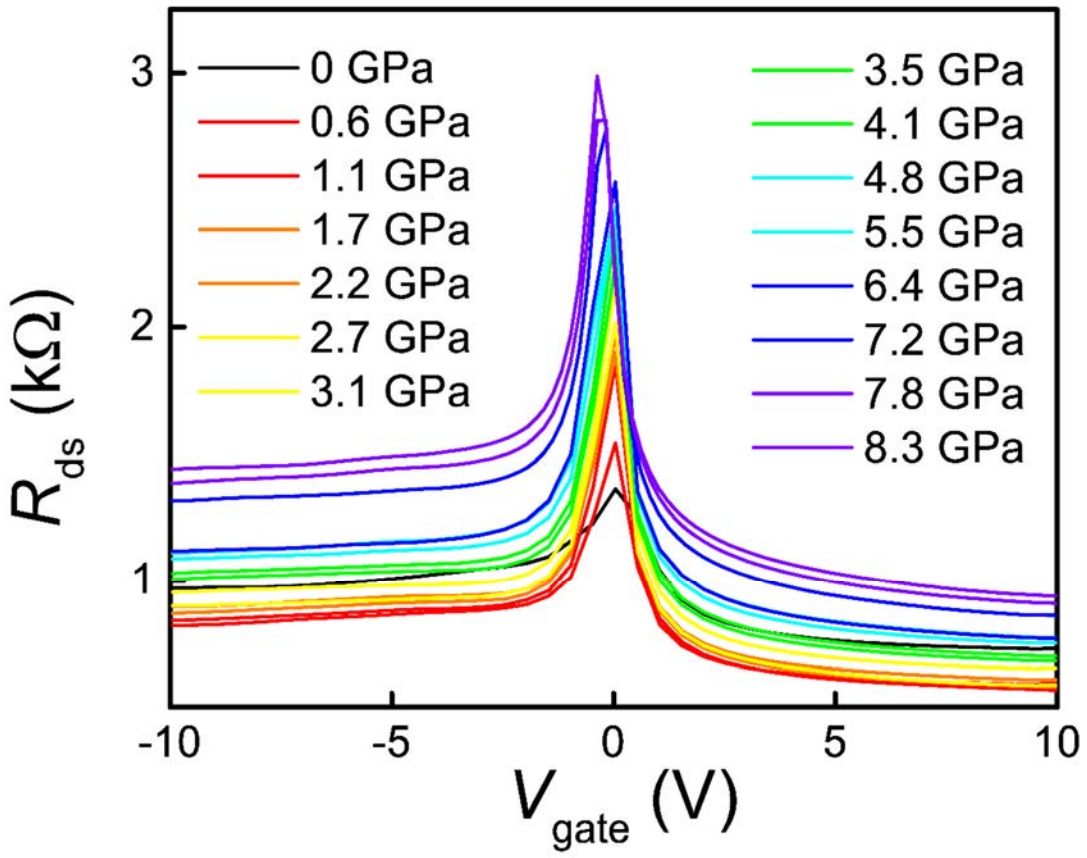

FIG. S3. Complete transfer curves of the device in the main text.

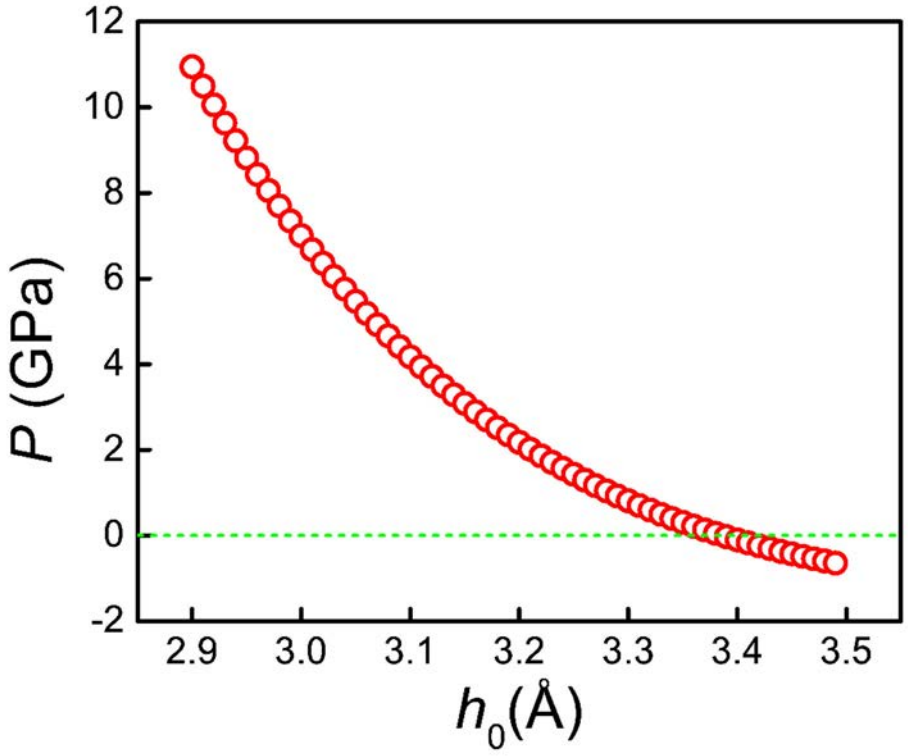

FIG. S4. Calculated interlayer space vs. pressure. The initial interlayer space is set to be 0.34 nm at 0 GPa.

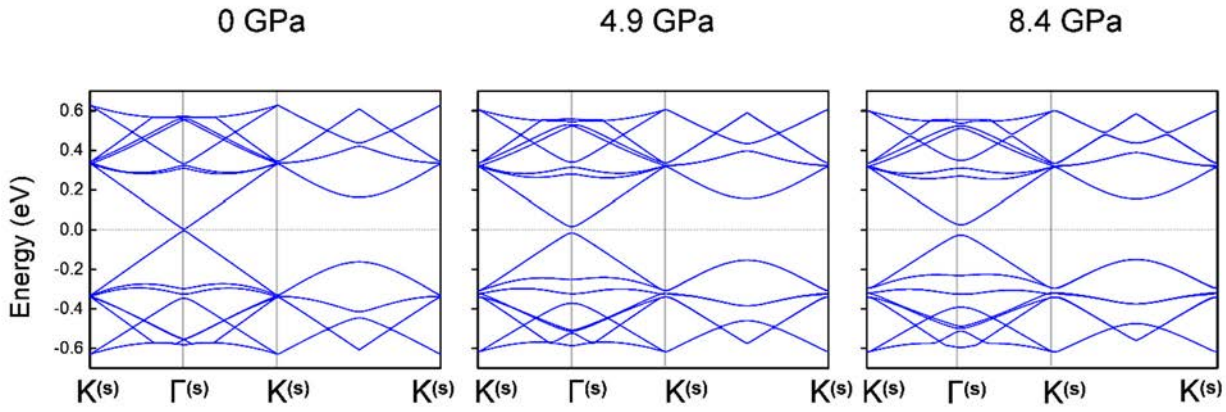

FIG. S5. Complete band diagrams of the 1.8° twist graphene moiré superlattice under pressure. The corresponding pressures are labeled. The bands on the hole side are overlapped at 0 GPa and 4.9 GPa and split slightly by 4.7 meV at 8.4 GPa. No secondary gap emerges in the conduction band.

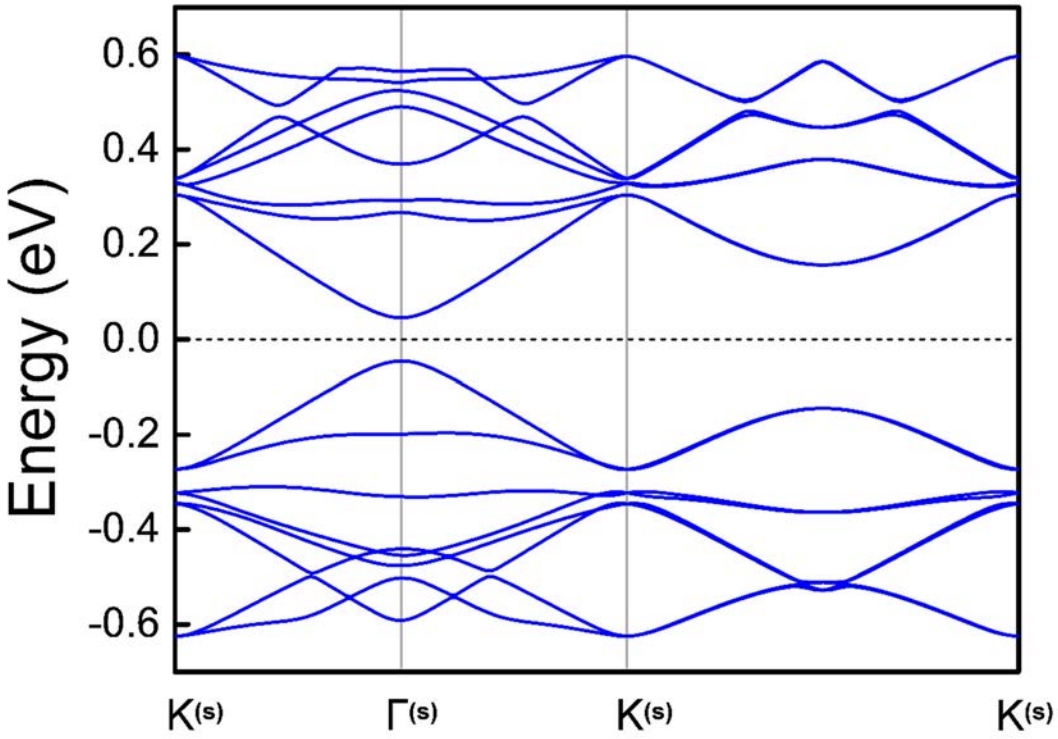

FIG. S6. The band diagram under 16.4 GPa. The SDP gap in the valence band remains indirect while the bands on the electron side are still overlapped, indicating no SDP gap.

Note 1. Device preparation and characterization

Graphene and h-BN were mechanically exfoliated onto the SiO_x/Si wafer (285 nm oxidation layer) using the conventional Scotch tape method. The monolayer graphene was found by optical contrast and confirmed with Raman measurement. h-BN flakes with thickness of 40-80 nm and clear straight crystalline edges were picked up by poly propylene carbonate (PPC) stamp [1,2]. The monolayer graphene with straight crystalline edge was identified, aligned the graphene edge to the h-BN edge on PPC optically and picked up with the help of the strong vdW attraction between graphene and h-BN. Then Raman mapping was performed with the prepared graphene/h-BN stack on PPC to verify the alignment angle. Particularly, FWHM > 25 cm^{-1} for the graphene 2D peak near 2700 cm^{-1} indicates an alignment angle ~1.8° [3]. The micro-Raman measurements were carried out using the commercial Renishaw Raman system, and the laser wavelength was 488 nm. The bottom graphite gate, bottom dielectric h-BN and drain/source graphite were exfoliated onto the PPC/SiO_x/Si substrate instead of the SiO_x/Si wafer. The PPC/SiO_x/Si substrate was prepared by spin coating PPC film onto a SiO_x/Si wafer. The thickness of the bottom graphite gate, bottom dielectric h-BN and drain/source graphite were pre-selected to be 30-60 nm and confirmed by atomic force microscope (AFM) before transferring to the diamond culet. The PPC film with ready-to-transfer graphite or h-BN flake was then carefully peeled off from the SiOx/Si wafer and placed onto a polydimethylsiloxane (PDMS) stamp for the transfer to diamond culet. The device and diamond culet were rinsed quickly with acetone to remove the possible PPC residues after each transfer. The electrodes were patterned by following the standard photolithography and lift-off process but using a specifically customized PL set-up. The Ti/Au films as the inner electrodes were deposited by electron beam evaporation with a vacuum level of 10^{-6} Torr.

Note 2. Transport measurements in the DAC

Hydrostatic pressure was generated by a symmetric DAC with 300 μm diameter culets (type IA diamond). Stainless-steel gaskets were pre-indented by DAC within 50 μm thickness, and a hole of ~200 μm was drilled by laser in the middle of the indented area. c-BN powder and epoxy gel were thoroughly mixed with the mass ratio of 10:1 [4] and placed onto the pre-indented ~200 μm gasket hole. The gaskets with the c-BN/epoxy composites were then indented again by DAC to < 50 μm thickness and laser-drilled a hole of ~100 μm as the sample chamber. Daphene 7373 was used as the pressure-transmitting medium because it was previously confirmed that Daphene 7373 had no significant impact on the transport properties of 2D materials [5,6]. The pressure was calibrated by the photoluminescence spectrum of ruby particles placed inside the sample chamber [7]. The thickness of the Pt foil was 4-8 μm, and it was manually cut by a sharp blade into narrow strips (~30 μm) as the feedthrough wires.

Note 3. Details on the calculation methods

A. Relaxation of graphene/h-BN under pressure

The atomic and electronic structures of relaxed MLG/BN under pressure have been obtained with models based on ab-initio calculations. For the considered heterostructure with a relative twist angle of 1.8°, we use the geometry parameters of the moiré superlattices in Ref. [8].

Since the domains with different stackings in the moiré superlattices have rather distinct interlayer interaction and optimal interlayer distance, each layer is strained and corrugated in the relaxed superlattices. The perpendicular pressure can be applied to reduce the average interlayer distance (h_0) and the in-plane deformation and out-of-plane corrugation are also influenced. To obtain the optimum geometry of the relaxed superlattices under pressure, the system with a fixed h_0 is first relaxed to calculate the variation of its total energy (E_{tot}) with h_0. Then the pressure is obtained by differentiation of E_{tot} with respect to h_0 as

$$P = -\frac{1}{\Omega^{(s)}}\frac{dE_{tot}}{dh_0} \tag{1}$$

where $\Omega^{(s)}$ is the supercell area [9].

We have employed the continuum elastic theory to evaluate E_{tot} of a moiré supercell. E_{tot} as the sum of the elastic energy (E_{el}) in each layer and interlayer interaction energy (E_{int}) is a functional of the displacement fields $\boldsymbol{u}^{(n)}(\boldsymbol{r})$ with $n = 1$ for the bottom BN layer and $n = 2$ for the top MLG layer and the interlayer distance field $h(\boldsymbol{r})$. The elastic energy functional is given by [10]

$$E_{el} = \sum_{j=1}^{2}\int d\boldsymbol{r}\left\{\frac{\lambda_j+\mu_j}{2}\left(\frac{\partial u_x^{(j)}}{\partial x}+\frac{\partial u_y^{(j)}}{\partial y}\right)+\frac{\mu_j}{2}\left[\left(\frac{\partial u_x^{(j)}}{\partial x}-\frac{\partial u_y^{(j)}}{\partial y}\right)^2+\left(\frac{\partial u_y^{(j)}}{\partial x}+\frac{\partial u_x^{(j)}}{\partial y}\right)^2\right]\right\}^2 \tag{2}$$

where the integral extends over a moiré supercell. The calculated 2D elastic Lamé factors are $\lambda_1 = 1.779$ eV/Å^2 and $\mu_1 = 7.939$ eV/Å^2 for BN and $\lambda_2 = 3.653$ eV/Å^2 and $\mu_2 = 9.125$ eV/Å^2 for MLG. The E_{int} is given by the integral of the local interlayer interaction energy

$$E_{int} = \int V[\boldsymbol{d}(\boldsymbol{r}), h(\boldsymbol{r})]\, d\boldsymbol{r} \tag{3}$$

where $\boldsymbol{d}(\boldsymbol{r}) = S^{-1}\boldsymbol{r} - \boldsymbol{r} + \boldsymbol{u}^{(2)}(\boldsymbol{r}) - \boldsymbol{u}^{(1)}(\boldsymbol{r})$ is the local shift vector for a relaxed superlattice with S denoting transformation of BN with respect to MLG [8]. The local interlayer interaction potential $V(\boldsymbol{d}, h)$ is obtained by *ab initio* calculations of bilayers with a constant shift vector $\boldsymbol{d}$ and interlayer distance h. In view of the rotational and periodic relations of the shifted bilayers, we express $V(\boldsymbol{d}, h)$ as

$$V(\boldsymbol{d}, h) = \tilde{V}_0(h) + \tilde{V}'(h)\sum_{j=1}^{3} cos(\boldsymbol{G}_j \cdot \boldsymbol{d}) + \tilde{V}''(h)\sum_{j=1}^{3} sin(\boldsymbol{G}_j \cdot \boldsymbol{d}) \tag{4}$$

where the sum is limited to three shortest vectors, $\boldsymbol{G}_1 = \boldsymbol{b}_1$, $\boldsymbol{G}_2 = -\boldsymbol{b}_1 + \boldsymbol{b}_2$, and $\boldsymbol{G}_3 = -\boldsymbol{b}_2$. $\boldsymbol{b}_i$ $(i = 1,2)$ are basis vectors of the reciprocal lattice of graphene whose Bravais lattice is spanned by $\boldsymbol{a}_1 = a(1,\ 0)^T$ and $\boldsymbol{a}_2 = a(-1/2,\ \sqrt{3}/2)^T$. The dependence of $\tilde{V}_0$, $\tilde{V}'$, $\tilde{V}''$ on h can be obtained from the variation of V with h for the AA-, AB-, and BA-stacked bilayers with $\boldsymbol{d}_{AA} = 0$, $\boldsymbol{d}_{AB} = (\boldsymbol{a}_1 + 2\boldsymbol{a}_2)/3$, and $\boldsymbol{d}_{BA} = -(\boldsymbol{a}_1 + 2\boldsymbol{a}_2)/3$ and are given by $\tilde{V}_0(h) = [V_{AA}(h) + V_{AB}(h) + V_{BA}(h)]/3$, $\tilde{V}'(h) = [2V_{AA}(h) - V_{AB}(h) - V_{BA}(h)]/9$, and $\tilde{V}''(h) = [V_{AB}(h) - V_{BA}(h)]/(3\sqrt{3})$. By ab-initio calculations of energies of bilayers, $V_{AA}(h)$, $V_{AB}(h)$ and $V_{BA}(h)$ are fitted as $V_{AA}(h) = 0.1086e^{-(h-3.2)/0.3232} - (2.048/h)^4 + 0.0965$, $V_{AB}(h) = 0.0880e^{-(h-3.2)/0.3136} - (1.995/h)^4 + 0.0909$, and $V_{BA}(h) = 0.0713e^{-(h-3.2)/0.3220} - (2.059/h)^4 + 0.1003$, with h and V in units of Å and eV per 4-atom unit cell, respectively, where the first terms represent the short-range repulsion and the second terms represent the long-range van der Waals interactions [11].

To relax MLG/BN with a fixed h_0, the $\tilde{\boldsymbol{u}}^{(n)}(\boldsymbol{r})$ and $h(\boldsymbol{r})$ have been expanded in Fourier series as

$$\boldsymbol{u}^{(n)}(\boldsymbol{r}) = \sum_{\boldsymbol{G}^{(s)}} \tilde{\boldsymbol{u}}^{(n)}(\boldsymbol{G}^{(s)}) e^{i\boldsymbol{G}^{(s)}\cdot\boldsymbol{r}} \tag{5}$$

and

$$h(\boldsymbol{r}) = h_0 + \Delta h(\boldsymbol{r}) = h_0 + \sum_{\boldsymbol{G}^{(s)}} \Delta\tilde{h}(\boldsymbol{G}^{(s)}) e^{i\boldsymbol{G}^{(s)}\cdot\boldsymbol{r}} \tag{6}$$

where the summation is over nonzero reciprocal lattice vectors $\boldsymbol{G}^{(s)}$ of the supercell. The total energy E_{tot} for a fixed h_0 is then minimized with respect to the expansion parameters by Euler-Lagrange equations [9].

B. Effective lattice Hamiltonian of graphene/h-BN

To calculate the band structures of relaxed MLG/BN under pressure, we adopt the effective lattice model of graphene moiré superlattices in Ref. [8] with model parameters directly extracted from the *ab-initio* electronic structure of shifted commensurate bilayers. This effective Hamiltonian is shown in the main text:

$$H = \sum_i (H_{A,i} c_{A,i}^\dagger c_{A,i} + H_{B,i} c_{B,i}^\dagger c_{B,i}) - \sum_i \sum_{n=1}^{3} t_{n,i} (c_{A,i}^\dagger c_{B,i,n} + c_{B,i,n}^\dagger c_{A,i}) \tag{7}$$

where $c_{\alpha,i}^\dagger (\alpha = A, B)$ is the creation and $c_{\alpha,i}$ is the annihilation operator of a p_z-like state at the site in the sublattice α and unit cell i of the MLG hexagonal lattice, $c_{B,i,n}^\dagger$ and $c_{B,i,n}$ are operators at the nearest sites of the sublattice-A atom in cell i, and the on-site energies and hopping terms are represented by $H_{\alpha,i}$ and $-t_{n,i}$, respectively. The hopping and on-site terms at a site with a local shift vector $\boldsymbol{d}$ were expanded in Fourier series, such as

$$t_n(\boldsymbol{d}) = \sum_{\boldsymbol{G}} \tilde{t}_n(\boldsymbol{G})\, cos[\boldsymbol{G}\cdot\boldsymbol{d} + \varphi_n(\boldsymbol{G})] \quad (8)$$

where $\boldsymbol{G}$ are reciprocal lattice vectors of MLG and $\tilde{t}_n(\boldsymbol{G})$ and $\varphi_n(\boldsymbol{G})$ are the expansion amplitude and angle [8]. Here, the Hamiltonian parameters also depend on the local interlayer distance h and are expressed as

$$t_n(\boldsymbol{d}, h) = \sum_{\boldsymbol{G}} [\tilde{t}'_n(\boldsymbol{G}, h)\, cos(\boldsymbol{G}\cdot\boldsymbol{d}) + \tilde{t}''_n(\boldsymbol{G}, h)\, sin(\boldsymbol{G}\cdot\boldsymbol{d})] \quad (9)$$

where $\tilde{t}'_n(\boldsymbol{G}) = \tilde{t}_n(\boldsymbol{G})\, cos[\varphi_n(\boldsymbol{G})]$ and $\tilde{t}''_n(\boldsymbol{G}) = -\tilde{t}_n(\boldsymbol{G})\, sin[\varphi_n(\boldsymbol{G})]$ for a given h. By calculating the expansion parameters for several different h, we find that they decay exponentially with h, such as

$$\tilde{t}'_n(\boldsymbol{G}, h) = \tilde{t}'_n(\boldsymbol{G}, h_P) e^{-(h-h_P)/\xi_n(\boldsymbol{G})} \quad (10)$$

where $\tilde{t}'_n(\boldsymbol{G}, h_P)$ and $\xi_n(\boldsymbol{G})$ can be calculated from the provided $\tilde{t}_n(\boldsymbol{G})$ and $\varphi_n(\boldsymbol{G})$ for both cases with constant interlayer distances of $h_P = 3.20$ Å and $h_N = 3.35$ Å in Ref. [8]. In addition, the effect of the local strain on the Hamiltonian parameters is also considered.

C. *Ab-initio* computational approach

The *ab-initio* density functional theory (DFT) calculations of pristine graphene and h-BN monolayers and the shifted bilayers were performed using the VASP code [12,13] to obtain the required model parameters. The local density approximation (LDA) [14] functional was adopted. The projector augmented wave (PAW) potentials [15,16] were used with a kinetic energy cutoff of 600eV. The BZ sampling was done using a 36×36×1 Monkhorst-Pack (MP) grid [17]. The vacuums in the *z* direction were larger than 17 Å. The tolerance for the energy convergence was 10^{-6} eV.

Note 4. Pressure-enhanced doping level

Graphene can be doped unintentionally during the device fabrication process by absorbates, chemical contaminations, Nitrogen or Boron atoms from h-BN [18-21]. Therefore, the transfer curves of graphene electronic devices sometimes display slight n- or p- type feature. Electrical field gating can shift the Fermi level of graphene and the lowest carrier concentration is reached when the Fermi level is in the middle point of the bandgap, which correlates with a resistance maximum at the PDP in the graphene moiré superlattices. The PDP slightly shifts into the negative gate voltage regime of the device in Fig. 2(b) at ambient, revealing negligible n-type doping. Unexpectedly, the PDP keeps moving towards left with pressure as shown in Fig. S7(a). Now we briefly derive the Fermi level shift based on the data set. Using the linear dispersion relation in graphene, we have the density of states (DOS):

$$g(E) = \frac{E}{\pi\hbar^2 v_F^2} \quad (11)$$

Using the Boltzmann approximation, we have the electron carrier concentration in conduction band:

$$n_e = \int_{E_C}^{\infty} g(E)\, e^{-(E-E_F)/kT} dE = \int_{E_C}^{\infty} \frac{E - E_C}{\pi\hbar^2 v_F^2} e^{-(E-E_F)/kT} dE$$

$$= e^{-(E_C-E_F)/kT} \int_0^{\infty} \frac{(E-E_C)d(E-E_C)}{\pi\hbar^2 v_F^2} e^{-(E-E_C)/kT} \tag{12}$$

$$= \frac{k^2T^2 e^{-(E_C-E_F)/kT}}{\pi\hbar^2 v_F^2}$$

Similarly, we have the hole concentration in the valence band:

$$n_h = \frac{k^2T^2 e^{-(E_F-E_V)/kT}}{\pi\hbar^2 v_F^2} \tag{13}$$

The primary Dirac peak is in the negative gate voltage regime, which means the Fermi level is slightly above the midpoint of bandgap (($E_C + E_V$)/2). The negative gate field will shift the Fermi level down to the midpoint, thus reaching the primary Dirac point, we have:

$$\sigma(V_g = 0V) \propto e^{-(E_c-E_F)/kT}$$

$$\sigma(PDP) \propto e^{-(E_c-E_V)/2kT} \tag{14}$$

$$\frac{\sigma(V_g = 0V)}{\sigma(PDP)} = e^{-(E_c+E_V-2E_F)/2kT}$$

Then the Fermi level shift can be estimated with the equation:

$$E_F - \frac{E_C+E_V}{2} = kT * e^{\frac{\sigma(V_{gate}=0V)}{\sigma(PDP)}} \tag{15}$$

E_F is the Fermi level, E_C and E_V are the conduction band minimum (CBM) and valence band maximum (VBM). If the bandgap middle point is set to be the zero-energy point, the Fermi level shift with pressure can be then plotted as well as E_C and E_V in Fig. S7(b). Fermi level monotonically shifts towards the CBM, illustrating heavier n-type doping. The original doping was usually unintentional, so it was quite difficult to experimentally determine the dopant source. Nonetheless, the possible doping mechanisms – absorbates, surface chemical contamination or h-BN could all be easily reinforced by enhancing the dopants – device interactions through vertical compressions. Therefore, the enhanced doping level is most likely induced by the pressure. It is noted that the pressure-activated doping enhancement is also applicable for original p-type device as shown in some previous reports but paid little attention [22,23].

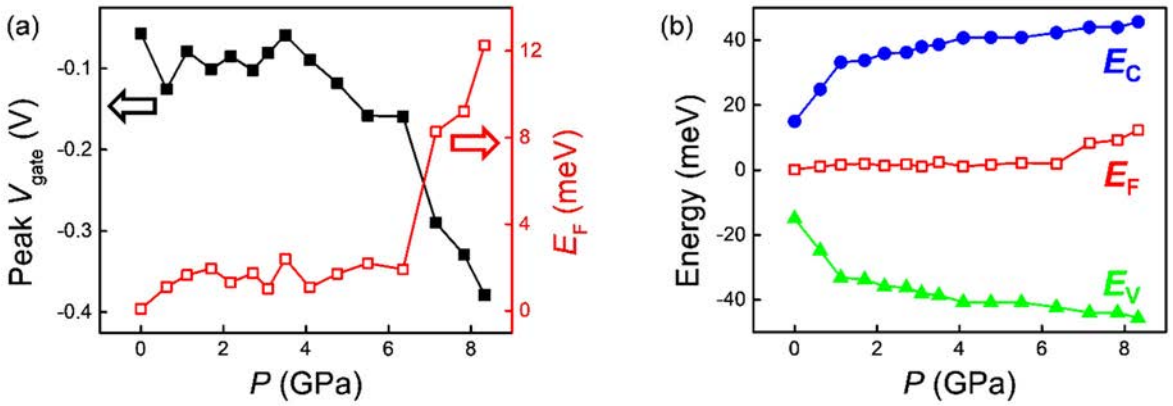

FIG. S7: Fermi level shift and bandgap opening under high pressure. (a) The primary Dirac point and the Fermi level shift in terms of pressure. The Fermi level is slightly n-doped at 0 GPa and monotonically shifting towards the hole doping side, indicating an enhanced n-type doping by pressure. (b) The conduction band minimum (CBM) and valence band maximum (VBM) evolution in terms of pressure. The bandgap is clearly opened by pressure and the Fermi level moves closer to the CBM and further to the VBM.

References

[1] K. Kim *et al.*, Nano Lett. **16**, 1989 (2016).

[2] K. Kim *et al.*, Proc. Natl. Acad. Sci. U.S.A. **114**, 3364 (2017).

[3] A. Eckmann *et al.*, Nano Lett. **13**, 5242 (2013).

[4] N. Funamori and T. Sato, Rev. Sci. Instrum. **79**, 053903 (2008).

[5] Y. Chen *et al.*, Nano Lett. **17**, 194 (2017).

[6] K. Yokogawa, K. Murata, H. Yoshino, and S. Aoyama, Jpn. J. Appl. Phys. **46**, 3636 (2007).

[7] A. D. Chijioke, W. J. Nellis, A. Soldatov, and I. F. Silvera, J. Appl. Phys. **98**, 114905 (2005).

[8] X. Lin and J. Ni, Phys. Rev. B **100**, 195413 (2019).

[9] X. Lin, H. Zhu, and J. Ni, Phys. Rev. B **101**, 155405 (2020).

[10] P. De Andres, F. Guinea, and M. Katsnelson, Phys. Rev. B **86**, 144103 (2012).

[11] S. Zhou, J. Han, S. Dai, J. Sun, and D. J. Srolovitz, Phys. Rev. B **92** (2015).

[12] G. Kresse and J. Furthmüller, Comput. Mater. Sci. **6**, 15 (1996).

[13] G. Kresse and J. Furthmüller, Phys. Rev. B **54**, 11169 (1996).

[14] J. P. Perdew and A. Zunger, Phys. Rev. B **23**, 5048 (1981).

[15] P. E. Blöchl, Phys. Rev. B **50**, 17953 (1994).

[16] G. Kresse and D. Joubert, Phys. Rev. B **59**, 1758 (1999).

[17] H. J. Monkhorst and J. D. Pack, Phys. Rev. B **13**, 5188 (1976).

[18] C. Zhang, L. Fu, N. Liu, M. Liu, Y. Wang, and Z. Liu, Adv. Mater. **23**, 1020 (2011).

[19] X. Wang, X. Li, L. Zhang, Y. Yoon, P. K. Weber, H. Wang, J. Guo, and H. Dai, Science **324**, 768 (2009).

[20] X. Dong, D. Fu, W. Fang, Y. Shi, P. Chen, and L.-J. Li, Small **5**, 1422 (2009).

[21] J. H. Chen, C. Jang, S. Adam, M. S. Fuhrer, E. D. Williams, and M. Ishigami, Nat. Phys. **4**, 377 (2008).

[22] M. Yankowitz *et al.*, Nature **557**, 404 (2018).

[23] K. Kinoshita, R. Moriya, M. Onodera, Y. Wakafuji, S. Masubuchi, K. Watanabe, T. Taniguchi, and T. Machida, npj 2D Mater.Appl. **3**, 22 (2019).